Supporting Information

Highly-Destabilized Ligand Field Excited States of Iron Carbene Complexes and Their Relation to Charge Transfer State Lifetimes

Reagan X. Hooper[a], Benjamin I. Poulter[a], Jesper Schwarz[b], Mariam Barakat[c], Kristjan Kunnus[d], Kacie J. Nelson[a], Aleksandra Ilic[b], Clara García-Mateos[b], Jens Uhlig[e], Kenneth Wärnmark[b], Elena Jakubikova[c], Amy A. Cordones[a], and Kelly J. Gaffney[a]*

[a]Stanford PULSE Institute, SLAC National Accelerator Laboratory, Menlo Park, CA 94025, United States.
[b]Centre for Analysis and Synthesis, Department of Chemistry, Lund University, Box 124, SE-22100 Lund, Sweden.
[c]Department of Chemistry, North Carolina State University, Raleigh, NC 27695, United States.
[d]LCLS, SLAC National Accelerator Laboratory, Menlo Park, CA 94025, United States.
[e]Division of Chemical Physics, Department of Chemistry, Lund University, Box 124, SE-22100 Lund, Sweden.

*Corresponding author email: kgaffney@slac.stanford.edu

Sections **Page**

Section I: Synthesis and General Experimental Methods

General Synthesis. All solvents for synthesis were used as received and were of synthesis grade, unless otherwise stated. Commercially available starting materials were purchased from Acros, Merck, or Fischer Scientific. NMR spectra were recorded at ambient temperature on a BrukerAvance 500 MHz NMR, equipped with a QCI CryoProbe. Chemical shifts (δ) for ^{1}H NMR spectra are reported in parts per million (ppm), relative to the residual solvent peak: CD_3CN (δ_H = 1.94 ppm).[1] Coupling constants (*J*) are given in Hertz (Hz), with the multiplicities being denoted as follows: singlet (s), doublet (d), triplet (t), quartet(q), multiplet (m), broad (br). Complexes **1a** and **2** were synthesized according to literature procedure.[2, 3] Ferrous **1a** is air sensitive and was stored and handled in an N_2-filled glove box with an O_2 concentration less than 1 ppm.

Complex [1b]BPh$_4$. A saturated solution of [**1b**]PF_6 (69.2 mg, 0.10 mmol)[3] in methanol was layered with a saturated solution of $NaBPh_4$ (69.8 mg, 0.20 mmol) in methanol. The combined solutions were left to crystallize overnight, and the resulting crystals were filtered off with a glas frit filter (#4) and washed with methanol (4 * 4 mL) to give pure [**1b**]BPh_4 (68.4 mg, 79%) as dark blue crystals. ^{1}H NMR (500 MHz, CD_3CN) δ (ppm) = 25.02 (s, 4H), 9.77 (s, 12H), 7.31 – 7.21 (m, 8H), 6.97 (t, *J* = 7.4 Hz, 8H), 6.86 – 6.79 (m, 4H), 2.79 (s, 4H), -2.56 (s, 4H), -36.41 (s, 2H).

XAS and RIXS Data Acquisition. Fe L-edge XAS and RIXS measurements of solid samples were measured at the Advanced Light Source (ALS), Lawrence Berkeley National Laboratory, beam line 8.0.1, with a beam spot size of 100 × 35 μm. With these beam dimensions, the resolving power of the monochromator and emission spectrometer is ~2000. To prepare the samples for measurement, they were ground into a fine powder then pressed onto conductive adhesive carbon tape and transferred to the beam line without exposing **1a** to air. The sample chamber was evacuated to 10^{-9} Torr prior to all measurements. The $L_{3,2}$-edge XAS spectra were acquired in total electron yield (TEY) mode after de-focusing the beam such that the X-ray photon flux was reduced to ~50% of its maximum. This was required to minimize beam damage, which may be problematic at high-flux RIXS beam lines. Monochromator energies were calibrated using solid $K_3[Fe(CN)_6]$.[4] The total X-ray exposure time of each sample during XAS ranged from 65 to 120 s, depending on observed damage, and a new spot was selected for each serial XAS measurement. Only one XAS scan per complex is reported, as sequential scanning often resulted in spectral changes, specifically in the low-energy region associated with t_{2g} transitions (Figure S1). The lack of t_{2g} feature in the least-sample-damaged XAS spectrum of **1a** (as expected) and

the single, sharp t_{2g} features in the least-sample-damaged spectra of **1b** and **2** suggest that the spectra we analyzed contain only minimal distortions due to sample damage that should not affect our interpretation (Figure S1, blue traces). RIXS spectra were acquired using the high-resolution RIXS spectrometer in fluorescence detection mode with a fully-focused beam. The samples were dithered over ~3 mm vertical distances during RIXS scanning, and the dither area was changed between each set of scans to reduce sample damage. For RIXS spectra at constant incident energies, five scans with 180 s accumulation times were averaged (there was negligible signal difference in each scan due to slight sample inhomogeneity). 2D RIXS maps were taken over the Fe L_3 edge using 90 s accumulation times. Partial fluorescence yield (PFY) spectra had reasonable agreement with the XAS TEY spectra (Figures S4–S6), suggesting that the XAS is representative of a sample with minimal beam damage (though some differences between TEY and PFY are normal due to differences in decay channels contributing to fluorescence signal compared to absorption).[5] The relatively strong elastic line of **1b** was used to calibrate the pixel to energy ratio for the 2D and constant incident energy (CIE) RIXS spectra, and a value of 0.2 eV per pixel was found, consistent with a previous RIXS study done at the same beam line.[6]

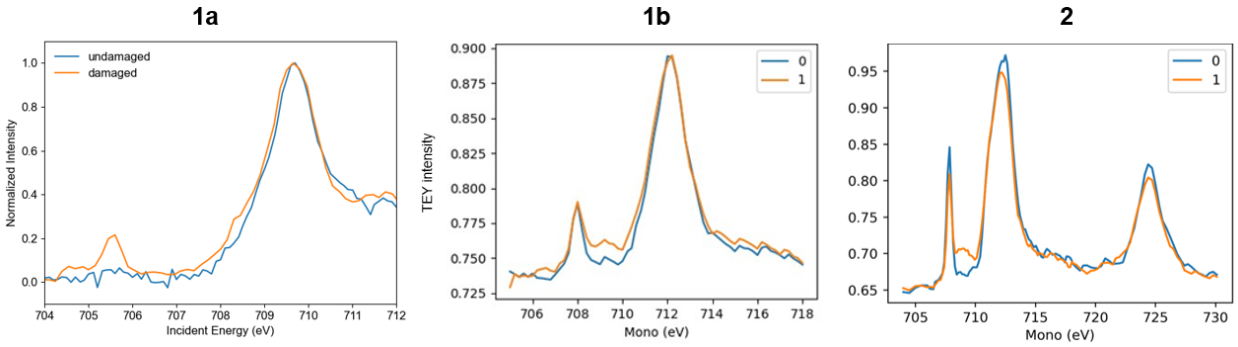

Figure S1. Total electron yield XAS spectra showing spectral signs of beam damage (orange traces) compared to spectra we analyzed with minimal beam damage (blue traces). The L_3 edge is shown for **1a** and **1b** while the L_3 and L_2 edges are shown for **2**.

Section II: Incident Energy Choice for Fitted RIXS Spectra.

Compared to projecting a RIXS spectrum at constant energy directly from the 2D RIXS map, choosing a constant incident energy and averaging several 1D RIXS spectra acquired at that energy can improve signal-to-noise, allowing for more accurate fitting. Intensities of RIXS features in the cuts are dependent on incident energy, as different intermediate states are accessed

by different absorption energies. Importantly, however, ligand field (LF) excited state energies are *independent* of the incident energy because the energy of the final states accessed do not depend on the specific intermediate state excited in the energy range associated with the e_g* resonance, only the relative amplitudes of the states.[7, 8] The dependence of final LF excited state intensities on incident energies means that with more complicated L-edge absorption spectra (like that of **2**), CIEs should be more carefully considered in the context of which intermediate states are accessed. In such cases, it is also valuable to acquire a full 2D RIXS spectra to capture a complete picture of the LF final states.

With the XAS and 2D RIXS maps in hand to provide resonant X-ray absorption energies, the following general methods were used for choosing CIEs: For ferrous **1a**, there is one major L_3-edge XAS feature at 709.7 eV (Figure 3), and thus RIXS fitting was done using a spectrum with an incident energy corresponding to the L_3-edge XAS maximum absorption, consistent with the protocol used in prior literature.[6, 9] The number of RIXS final states is relatively limited across this region for ground state d^6 ions, and therefore no additional CIEs were evaluated. Similar to ferrous **1a**, ferric **1b** also has a well-defined absorption resonance at 709.7 eV in the XAS spectrum (Figure 3), and the RIXS spectrum at 709.7 eV was also used to fit LF excited state energies of **1b**. For the more spectrally-complicated ferric **2**, an energy that likely accesses the same intermediate states as those accessed by exciting into the peak absorption of **1b** was chosen, at 709.6 eV (Figure 4). Further comments regarding a consistent CIE choice between ferric complexes **1b** and **2** can be found in the section below.

Section III: Discussion of Ferric L_3-Edge Multiplets

Shape of the Ferric e_g* Absorption Region. The two ferric complexes in this study display markedly different spectral features upon L-edge excitation into the e_g* orbital set to form $(2p)^5(3d\ t_{2g})^5(3d\ e_g^*)^1$ configuration based states (Figure 3). Literature Fe L-edge XAS spectra of other low-spin iron(III) complexes also demonstrate a broad e_g* feature, many of which are asymmetric with a low-energy shoulder as seen for **2**.[4, 7, 9, 10] One such study comparing an iron(III) complex with nearly-degenerate e_g* orbitals to one with non-degenerate e_g* orbitals suggests that it is not descent in symmetry that dictates the overall shape of the e_g* XAS region.[11] While CT resonances may appear as weak or strong satellite features in the XAS, the pervasive low-energy shoulder is likely not assignable to a CT absorption, as it is present in the spectrum of $[Fe(tacn)_2]^{3+}$

(a cyclic amine ligand lacking the π interactions that usually give rise to low-lying CT states).[11] Next, the ferric XAS shape was considered in d^6 ligand field theory formalisms, as the final states produced by Fe 2p → Fe 3d absorption have six valence d electrons. The d^6 LF ES energies show a dependence on Racah *B* and *C* for the four lowest excited states, and so the impact of changing these parameters on these state energies (and thus the L_3-edge XAS spectrum for a d^5 ion) was simulated by scaling the Slater integrals F_{dd}.[12] The splitting is mainly due to divergence of the $^3T_1$ and $^3T_2$ energies at F_{dd} values closer to the free ion. Spectral shape differences between the two ferric complexes **1b** and **2** in our study suggest that, in the absence of strong CT effects, the shape of the e_g* region at the Fe L_3 absorption edge may be used as a qualitative fingerprint of covalency. Specifically, the unusually sharp e_g* band for **1b** indicates that it is more covalent (F_{dd} is smaller) than **2**, which is supported below by detailed analysis of the LF excited state energies in the RIXS spectra. More general figures showing the dependence of the LF ES energies on F_{dd} scaling are shown in Figure S7, which were generated using CTM4DOC.[13]

Choice of RIXS Incident Energies for Ferric LF Excited State Fitting. Using the information above regarding a first-order model for differential iron(III) L-edge XAS spectra, we sought a consistent method for picking incident energies at which RIXS spectra for LF excited state fitting would be measured. The choice of incident energy does not affect the LF excited state energies, and therefore any CIE along the interest region can access the same final LF excited states.[14] However, the relative intensities of various LF final states *are* influenced by the CIE choice, and therefore we aimed to access the same analogous intermediate RIXS states in **1b** and **2** for fit consistency purposes. For **1b**, the targeted L-edge resonant absorption was fairly clear due to its single maximum in the e_g* absorption region (Figure S5). The model above predicts that this absorption maximum is likely a mixture of $^3T_1$ and $^3T_2$ L-edge valence final states (Figure 4) that appear as a single resonance at 709.7 eV due to their energetic closeness. For **2**, this same excitation energy intermediate to those two states is approximately between the tallest peak and its low energy shoulder, corresponding to the dark blue vertical trace at 709.7 eV in Figure 5. Thus, RIXS fitting was done at the peak absorption energy of 709.7 eV for **1a** and at 709.7 eV for **2**, corresponding in both to an incident energy that likely produces primarily a mixture of $^3T_1$ and $^3T_2$ intermediate states (recall this is in the d^6 formalism, neglecting the 2p hole).

Ligand Field Multiplet Simulations. The CTM4XAS55[15] program was used to simulate the effects of different degrees of F_{dd} reduction on Fe L-edge XAS, shown in Figure 4. To isolate

the effect of changing F_{dd} on the LF multiplets, the following parameter settings were all set to zero; i.e., they were not included in the model: Slater integrals F_{pd} and G_{pd} and valence spin-orbit coupling. Additionally, the simulations did not include charge transfer state mixing. Core hole spin-orbit coupling was preserved at its full value, and the O_h point group with 10Dq equal in the initial and final states was used. Only the F_{dd} parameter was adjusted to give the traces in Figure 4, with a value of 1 corresponding to the free ion (80% Hartree-Fock) value, 0.75 corresponding to '75% Scaling,' and 0.5 corresponding to '50% Scaling' of the free ion value.

Section IV: Further Discussion of RIXS Modeling Method

Justification for Modeling Method. Within the LF framework, two main fitting options exist. The first is that three LF peaks can be manually selected and their energies inserted into Tanabe-Sugano matrices such that all LF parameters are solved. This method relies on the ability to both resolve and assign individual peaks. The second option, which we utilized, is to assume nothing about peak positions and to perform a fit that allows the parameters 10Dq, *B*, and *C* to float *while maintaining the constraint that the energies must conform to the Tanabe-Sugano matrices.*[9, 16] The first option can give a unique set of parameters within the prescribed assumptions, but we chose the second option because the intrinsic broadening in the spectra combined with the spectral resolution (~0.3 eV) in our study does not enable the distinct LF excited states to be resolved in the RIXS spectra.

General Fitting Details. Our initial pixel-to-energy calibration using the elastic line of a 2D RIXS map generally placed the elastic lines of the CIE RIXS cuts at zero, and we also made fine adjustments when needed (< 0.1 eV) to ensure that the center of the elastic line was at zero for the purposes of setting it as the electronic ground state. Individual excited states were fit as Gaussian curves, and the fit was maximized using least-squares fitting of the residual. This procedure was developed and described previously to fit the L-edge CIE RIXS spectra of an iron bis(diarylamido) complex, and it has the advantage of not requiring a large semi-constrained parameterization space that is often required for commonly-used charge transfer multiplet (CTM) calculations.[9] Although the complexes herein are not strictly O_h in symmetry, treating them as such is within the bounds of spectral resolution and is set by literature precedent for complexes with a similar degree of distortion from O_h symmetry. Metal-ligand bond lengths maximally span ~0.05 Å in **1b** and ~0.02 Å in **2**, while they are all indistinguishable in **1a**. Bond angles are near 90° for **2** and are comparable to other iron complexes that have been successfully analyzed within the O_h

point group.[6, 9] To greatly reduce the variable space, Gaussian fit line widths were fixed to a single floated value for the inelastic scattering region (i.e., LF states), while a separate width was allowed for the elastic scattering band.

Fixed vs. Floated *C*/*B*. The LF energies may be fit assuming a fixed or floated *C*/*B* ratio (where *C* and *B* are Racah parameters). While the former is commonly employed, particularly when necessitated by only two experimentally-identifiable LF ES energies, there is no physical reason to fix the *C*/*B* ratio to the free ion value of 3.73.[17] On the contrary, there *is* a physical argument for different complexes having different *C*/*B* ratios.[17] As thoroughly described by Schmitdke, the distinct dependencies of *B* and *C* to F^2 and F^4 and the distinct radial distance dependence of F^2 and F^4, presume a distinct dependence of *B* and *C* to the nephelauxetic effect or metal-ligand covalency, not a constant ratio for *C*/*B*.[17] Since both parameters change by different magnitudes when the d-electron wavefunction changes (as it does between different complexes), it is sensible to use a model in which F^2 and F^4 can be independently scaled. As a result of enabling differential F^k_{dd} scaling, *C*/*B* can also change between complexes, and variable *C*/*B* has been shown to provide improved RIXS fits when the differences from the fixed *C*/*B* fit are clearly discernable.[7, 8] When *C*/*B* is floated, we argue that the nephelauxetic parameter $\beta = B_{complex} / B_{free\ ion}$ is not meaningful for comparison between complexes that have different *C*/*B*. The reason is because under this model, $B_{complex}$ itself is no longer independent of *C*/*B*, as can be seen from Equation S3, where the equation $x = C/B$ was solved for *B*, and *C* was substituted with Equation S2.

$$B = F_2 - 5\,F_4 = \left(\frac{1}{49}\right) F^2 - 5\left(\frac{1}{441}\right) F^4 \qquad \textbf{Equation S1}$$

$$C = 35\,F_4 = 35\left(\frac{1}{441}\right) F^4 \qquad \textbf{Equation S2}$$

$$B = \left(\frac{1}{49}\right)\left(1 + \frac{5}{35}x\right)^{-1} F^2 \text{, where } x = C/B \qquad \textbf{Equation S3}$$

Uncertainty Estimations. To estimate uncertainty in the LF parameters in the large parameter space when *C*/*B* is floated, we bootstrapped the residual of the initial least-squares fit to

sample alternative RIXS spectra fit solutions. In this procedure, the initial residual was defined as the difference between the RIXS data and the total fit, and this was obtained from the fits shown in Figure 6. All of the points in the initial residual were then randomly re-sampled to form a new residual, which was used to create an artificial RIXS spectrum by adding the re-sampled residual to the initial fit. Least-squares fitting was then used on the artificial data to obtain to obtain new LF parameters. The number of bootstrap iterations was 1000, and the results of this sampling are shown in Table S5.

Section V: Further Discussion of Racah Parameters and Covalency

We used values of $B_{\text{free ion}}$ that were originally reported by Tanabe and Sugano (917 cm^{-1} (ferrous) and 1015 cm^{-1} (ferric)), which are close to alternatively-used B_0 values that are equal to 80% of the Hartree-Fock calculated B for the free ions (945 cm^{-1} (ferrous) and 1035 cm^{-1} (ferric)).[18, 19] The β parameter (for C/B = 3.73) for **1a** is 0.63. This is lower than β for its pyridine analogue **3**, where the value is 0.75 (obtained by dividing the reported Hartree-Fock Slater scaling by 0.8 to reflect the value of B_0 being 80% of the full Hartree-Fock B).[6] The B value for floated C/B, 346 cm^{-1}, is much lower than that of other iron(II) complexes.[7, 20] Considering iron(III) complexes **1b** and **2**, β (for C/B = 3.73) is reduced for **1b** (0.43) relative to **2** (0.50), indicating that **1b** is more covalent (Table 1). The β value for **1b** is also lower than that of other octahedral iron(III) complexes in the literature.[6, 9]

The Racah parameters are themselves functions of more physically meaningful Slater integrals (F^k_{dd}), whose changes represent the degree of isotropic radial d electron expansion that occurs at a metal site upon formation of a metal-ligand bond.[17] A lower F^k_{dd} than the free-ion value is indicative of more diffuse d orbital wavefunctions and decreased metal d electron repulsion. Our RIXS fitting procedure gives the values of the F^2 and F^4 integrals, which are shown in Table S1. Major comparisons are only drawn between our two ferric cases, as differing free ion values of F^k_{dd} for different oxidation states make comparisons between ferrous and ferric complexes more tenuous. Similar to the β parameter, F^2 and F^4 are both reduced for **1b** relative to **2** and other iron(III) complexes in the literature.[21] The low F^2 and F^4 values allude to bonding that causes diminished interelectron repulsion in the valence metal orbitals through covalency effects.

Table S1. Scaling factors of F^k_{dd} from fitting of the Tanabe-Sugano diagrams. The scaling is relative to 80% of the Hartree-Fock F^2 and F^4 values (the 'free ion' values).

Complex	F^2 scaling	F^4 scaling	F^2 free ion (eV)	F^4 free ion (eV)
1a	0.585	1.000	8.773	5.452
1b	0.387	0.524	9.634	6.028
2	0.650	0.674	9.634	6.028

A survey of the F^k_{dd} parameters of other iron(III) complexes found trends suggesting that the ratio of F^2/F^4 correlates with differential σ and π bonding effects: a ratio near 2.0 was observed for complexes with ligands that have no π* orbitals, a ratio of 1.5 with ligands that have π* orbitals but lack a large conjugated π network, and a ratio between 1.1 and 1.3 with ligands that have a conjugated π system.[21] These relations appear to apply to our case. Complex **1b** has an F^2/F^4 ratio of 1.2 and a large π system that extends throughout the entire ligand, due to the coplanarity of both NHCs with the central phenyl group (Table S2). Since none of the NHCs in **2** are coplanar, π conjugation throughout the entire ligand is not possible (yet each NHC has π* orbitals), and it has an F^2/F^4 ratio of 1.5 (Table S2).

Table S2. Slater integrals as determined directly from RIXS spectra fitting. F^2 and F^4 are given in units of 1000 cm^{-1}.

Complex	F^2	F^4	F^2 / F^4
1a	41.4	44.0	0.9
1b	30.1	25.5	1.2
2	49.7	32.7	1.5

Additional spectroscopic evidence for increased covalency in **1b** relative to **2** is that **1b** displays a wide band of non-zero energy transfer features in its 2D RIXS map (Figure S5) at the incident energy (~705.5 eV) corresponding to final states which are likely of LMCT character (ligand to iron t_{2g}).[10] These states only gain intensity through mixing of metal d and ligand orbitals, and there is only one detectable analogous signal in the 2D RIXS map of **2** (Figure 5 and S6). Based on our LF analysis and Fe L_3-edge XAS, we also propose that the degree of splitting in the

XAS region of $(t_{2g})^4(e_g^*)^1$ states is another direct observable for assessing metal-ligand covalency in iron(III) complexes (Figure S1).

Section VI: Additional Figures and Tables

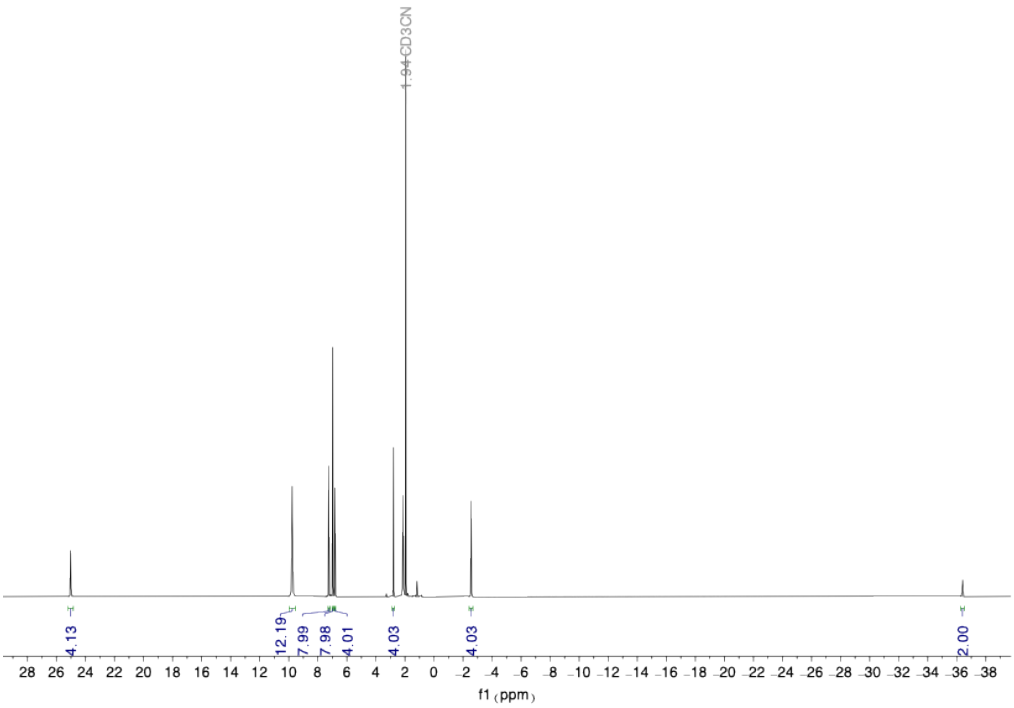

Figure S2. ^{1}H-NMR spectrum (500 MHz, $CDCl_3$) for compound [**1b**]BPh_4.

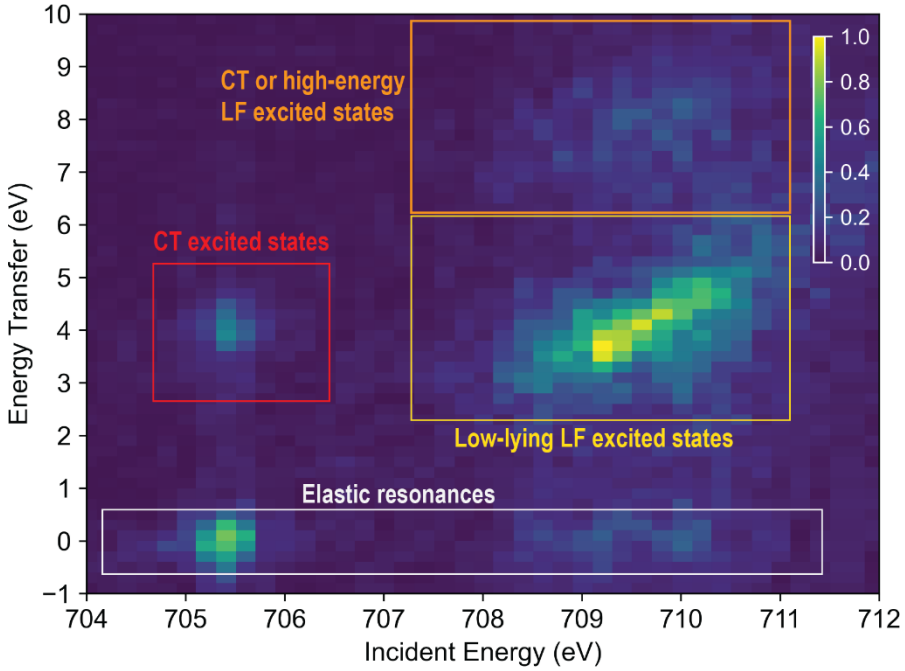

Figure S3. Dominant state assignments in the iron L_3-edge RIXS map of **2**.

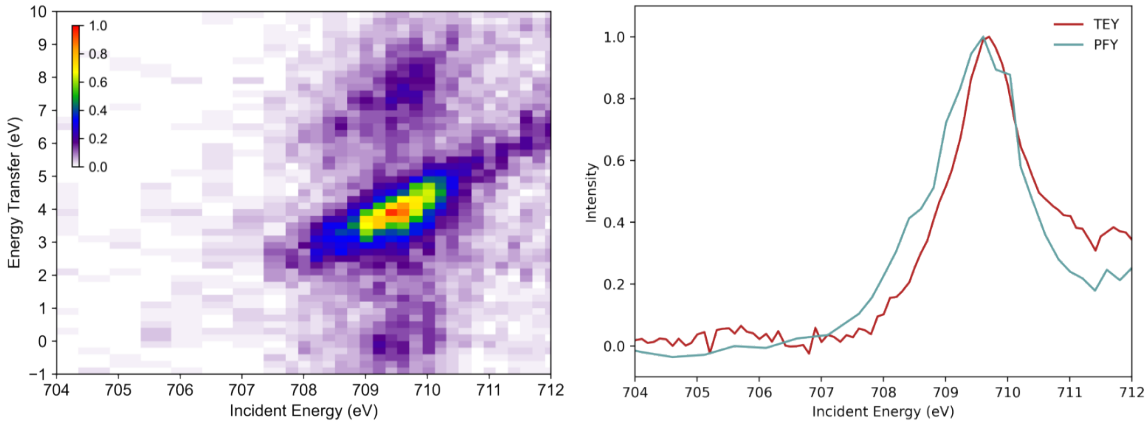

Figure S4. Intensity-normalized 2D RIXS map at the iron L_3 edge of ferrous complex **1a** (left) and corresponding partial fluorescence yield (PFY) obtained by integration of the 2D RIXS signals compared to the XAS TEY spectrum (right). The RIXS color scheme has been chosen to emphasize low-intensity features, and the colorbar indicates normalized RIXS intensity.

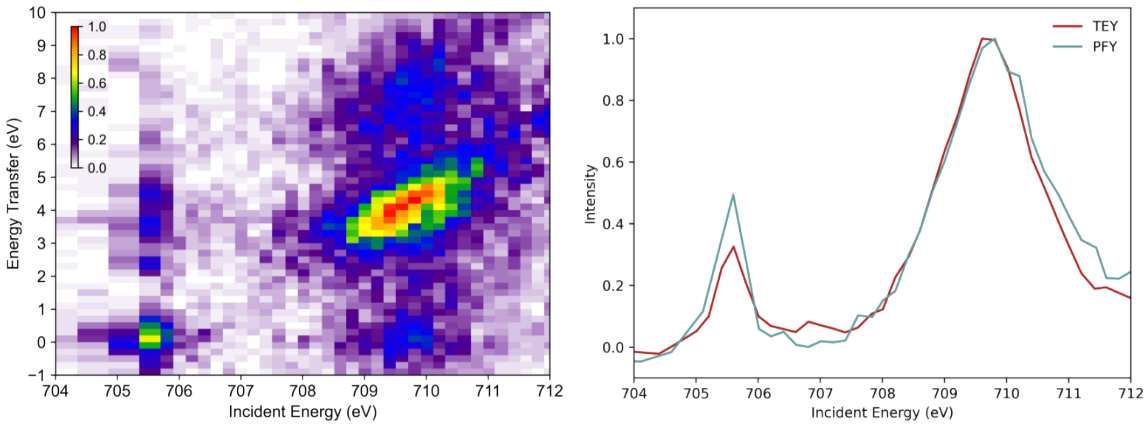

Figure S5. Intensity-normalized 2D RIXS map at the iron L_3 edge of ferric complex **1b** and corresponding partial fluorescence yield (PFY) obtained by integration of the 2D RIXS signals compared to the XAS TEY spectrum (right). The RIXS color scheme has been chosen to emphasize low-intensity features, and the colorbar indicates normalized RIXS intensity.

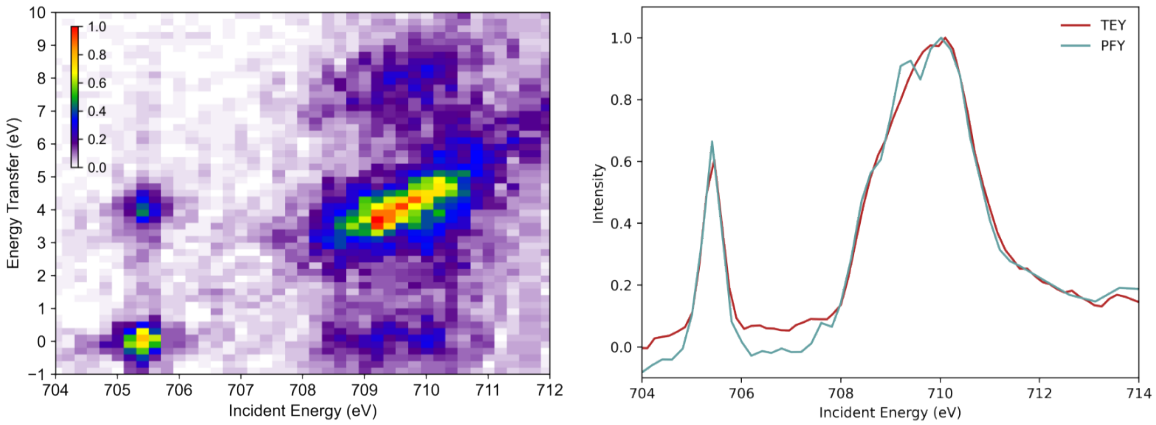

Figure S6. Intensity-normalized 2D RIXS map at the iron L_3 edge of ferric complex **2** and corresponding partial fluorescence yield (PFY) obtained by integration of the 2D RIXS signals compared to the XAS TEY spectrum (right). The RIXS color scheme has been chosen to emphasize low-intensity features, and the colorbar indicates normalized RIXS intensity.

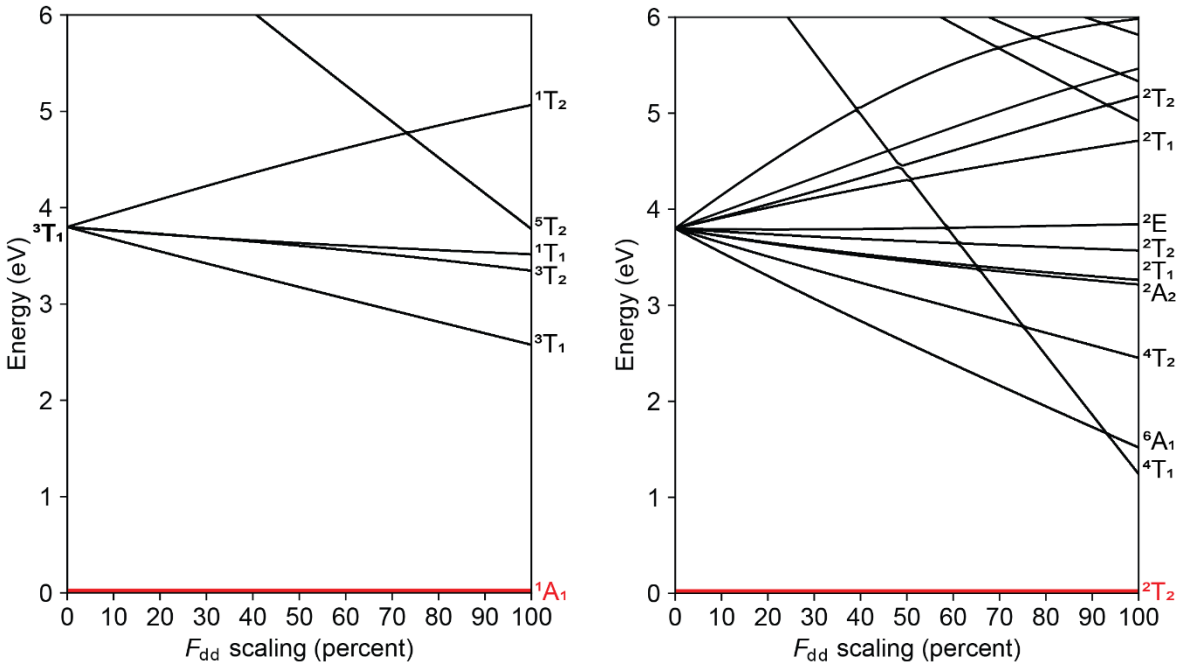

Figure S7. Ligand field ES energies for a d^6 (left) and d^5 (right) ions as a function of a uniform F^k_{dd} scaling (as opposed to scaling F^k_{dd} differently for different k), meaning that the C/B ratio is fixed and that the F^k_{dd} scaling is equivalent to the nephelauxetic parameter β. The value of 10Dq in these diagrams is 3.8 eV.

Table S3. Ligand field excited state term symbols and fitted energies for ferrous complex **1a**. Some terms have zero intensity in the fit and therefore do not appear in the visual fits. The bolded term is the most intense in the fit. The fitted energies are precise to approximately 0.05 eV, as determined by changes in the fitting parameter constraints that still gave reasonable fits ($R^2 \geq 0.99$). States with an asterisk have zero intensity in that fit.

Term (d^6)	Fitted Energy (eV) when $C/B = 10.1$	Fitted Energy (eV) when $C/B = 3.7$
$^1A_1$	0.00	0.00
$^3T_1$	3.35	3.65
$^3T_2$	3.66	4.17*
$^1T_1$	**4.23**	**4.21**
$^1T_2$	4.87	5.26

Table S4. Ligand field excited state term symbols and fitted energies for ferric complexes **1b** and **2**. Some terms have zero intensity in the fit and therefore do not appear in the visual fits. The bolded term in the most intense in the fit. The fitted energies are precise to approximately 0.05 eV, as determined by changes in the fitting parameter constraints that still gave reasonable fits ($R^2 \geq 0.99$). States with an asterisk have zero intensity in that fit.

	1b		**2**	
Term (d^5)	**Fitted Energy (eV) when $C/B = 6.2$**	**Fitted Energy (eV) when $C/B = 3.7$**	**Fitted Energy (eV) when $C/B = 4.0$**	**Fitted Energy (eV) when $C/B = 3.7$**
$^2T_2$	0.00	0.00	0.00	0.00
$^4T_1$	3.14	2.91	2.23	2.33
$^4T_2$	3.45	3.44	2.84	2.93
$^2A_2$	4.00	3.81	3.37	3.38*
$^2T_1$	4.12*	3.83*	3.39*	3.41
$^2T_2$	3.98*	4.03*	3.61*	3.63
^2E	**4.23**	**4.17**	**3.79**	**3.79**
$^2T_1$	4.54*	4.70	4.38	4.39
$^2T_2$	4.61*	4.87*	4.61*	4.62*
$^2A_1$	4.76	5.10	4.86	4.87
^2E	5.48	5.77	5.56*	5.53

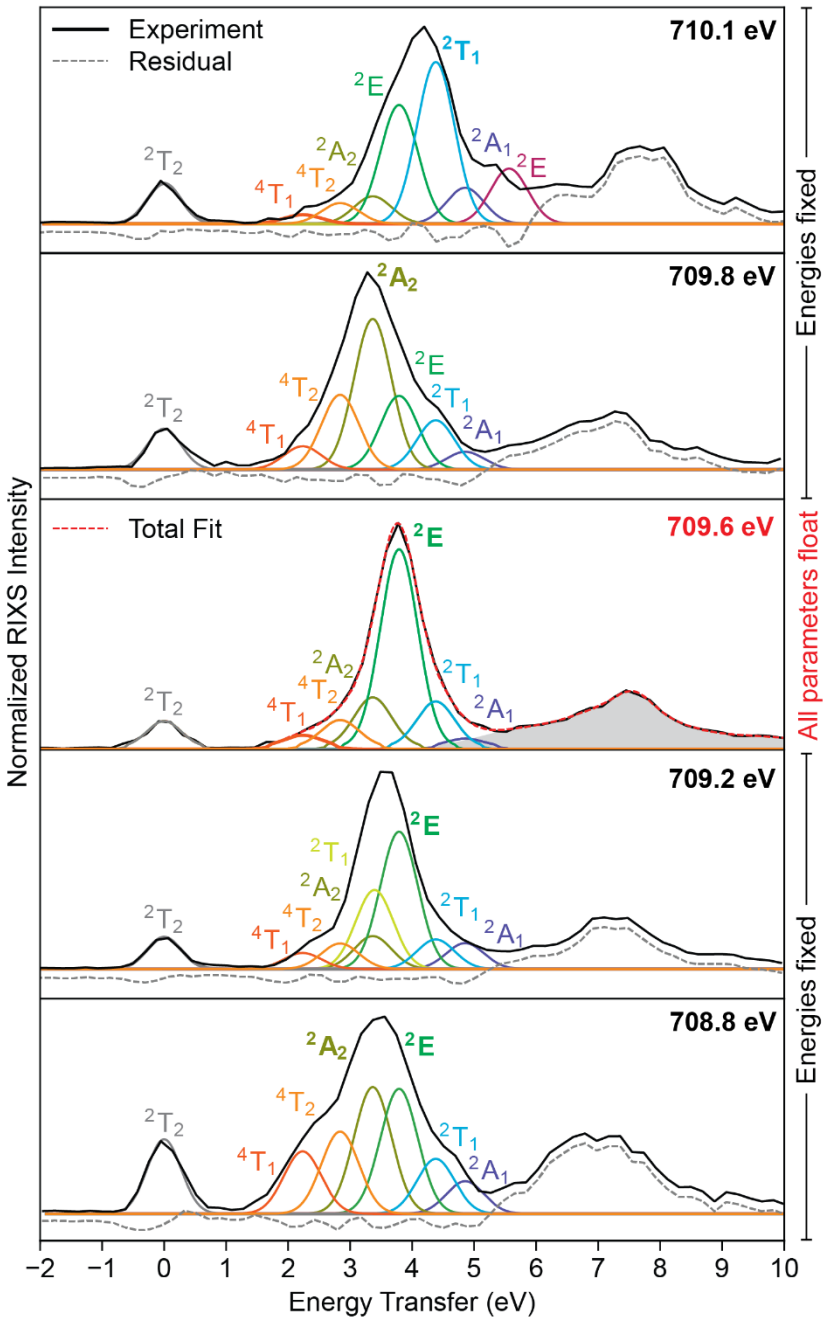

Figure S8. RIXS spectra of **2** obtained at different CIEs. In each of the windows, the fitted peak energies and line widths are constant, while amplitudes are variable. Peak energies are derived from the fit at 709.6 eV, where energy positions and line width was floated (all of the inelastic peaks were constrained to a single floated line width). The most intense LF ES term symbol in each spectrum is bolded. The grey area indicates CT or high-energy LF excited states.

Table S5. Bootstrap-derived (1000 samples) estimations for error in LF parameters due to fit procedure.

Parameter	Bootstrap standard deviation (σ) for floated *C*/*B*		
	1a	**1b**	**2**
10Dq (eV)	0.08	0.06	0.04
F^2 **scaling**	0.033	0.027	0.029
F^4 **scaling**	0.059	0.034	0.044
B **(cm^{-1})**	71	59	66
C **(cm^{-1})**	207	133	168
C*/*B	0.2	0.2	0.1

Section VII: DFT Calculations and Molecular Coordinates

All Complexes were optimized in their singlet (**1a**) or doublet (**1b** and **2**) ground state using the B3LYP functional,[22] and Grimme's D2 dispersion correction[23] in gas-phase. The Stuttgart/Dresden (SDD) effective core potential and its corresponding basis set were utilized for Fe,[24] while the 6-311G* basis set was employed for all other atoms (H, C, N).[25, 26] Geometric coordinates are provided in the SI. Vibrational Frequency analysis was performed to ensure that the optimized structures correspond to minima on their respective potential energy surface in gas-phase. Fragment molecular orbital (FMO) analysis as implemented in AOMix was performed to quantify the amount of MO localization on the metal (Fe).[27] All calculations on the molecular complexes were carried out using the Gaussian 16.C02 software package.[28]

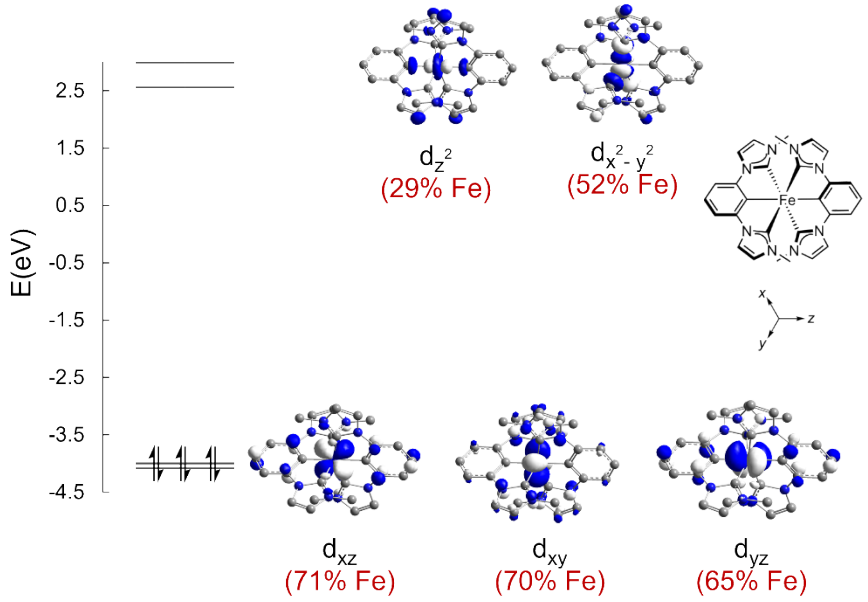

Figure S9. MO diagram of **1a** (singlet at ground state). % Fe describes the percentage of iron contribution to the specified orbital.

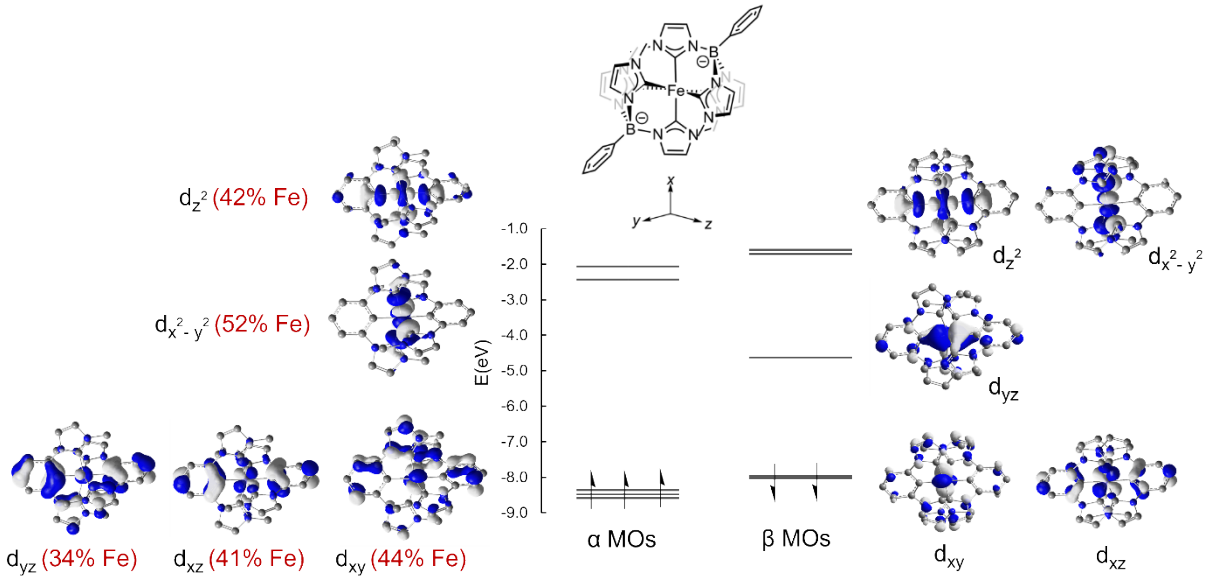

Figure S10. MO diagram of **1b** (doublet at ground state). % Fe describes the averaged percentage of iron contribution to the specified orbital in α and β sets of orbitals.

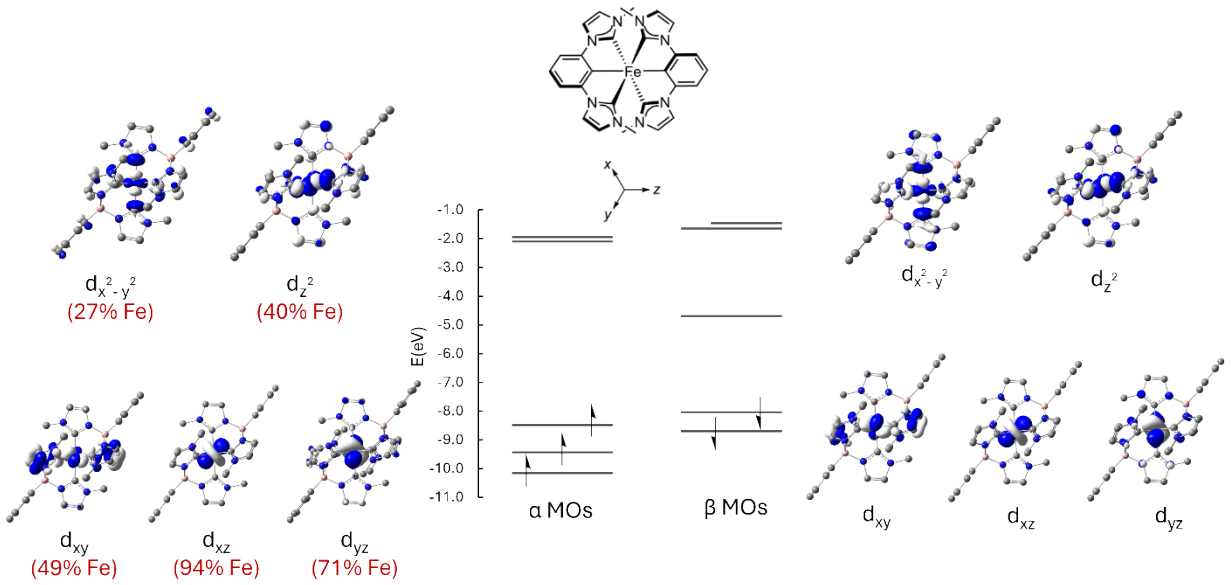

Figure S11. MO diagram of **2** (doublet at ground state). % Fe describes the averaged percentage of iron contribution to the specified orbital in α and β sets of orbitals.

Carsetian Coordinates of **1a**:

63
FeC28N8H26

Fe 4.10678431 4.18332228 9.00548440
N 2.74871383 1.34331136 9.14386945
C 2.50620020 0.95416168 6.98110093
C 4.02536341 4.33681669 4.26390057
C 3.54654368 3.19991755 6.31501449
C 2.29183919 0.41911028 8.20850042
H 1.85741435 -0.52341087 8.50151612
C 3.50502842 3.21102574 4.92216742
H 3.08906648 2.38804135 4.34654941
N 3.09001022 2.18885610 7.19615736
C 3.25623689 2.45802669 8.54774269
C 2.71785756 1.11805851 10.57876136
H 1.70848048 0.83459954 10.89058907
H 3.01009931 2.03893366 11.07579120
H 3.41600102 0.32210611 10.85632787
N 5.47890042 7.00706349 9.28014491
C 5.64999976 7.53407416 7.13990043
C 4.57760856 5.33840914 6.36648227
C 5.90948678 7.98786354 8.39108504
H 6.35851918 8.90823535 8.72906101
C 4.57004196 5.41792038 4.97528849
H 4.96667170 6.27693980 4.44009194
N 5.06697042 6.29006838 7.29489347
C 4.94612062 5.93437215 8.63126920
C 5.57118130 7.13413282 10.72435087
H 6.60617879 7.33164213 11.01863755
H 5.23614978 6.20191064 11.17072908
H 4.93576173 7.95275446 11.07629379
N 1.29988850 5.61105695 8.88691759
C 0.88981055 5.77944391 11.05287124
C 4.17792384 4.02967692 13.74715635
C 3.08792870 4.63313145 11.70345001
C 0.38304876 6.06908223 9.82895143
H -0.53807480 6.55114787 9.54246974
C 3.07447027 4.60466162 13.09665193
H 2.24921170 5.00764484 13.67820914
N 2.10281787 5.15485863 10.82915389
C 2.38649166 5.03773787 9.47533779
C 1.12388135 5.76400194 7.45295713
H 1.18215977 6.81994023 7.17093879
H 1.91602260 5.21566394 6.95070876
H 0.15093722 5.36535555 7.15137239
N 6.90693773 2.76970531 8.71028497
C 7.38287141 2.46245776 10.84730267
C 5.20595093 3.56140534 11.63700099
C 7.85196225 2.25321969 9.59231385
H 8.76357328 1.79179353 9.24737007
C 5.26097772 3.49922304 13.02795703
H 6.10287129 3.06022625 13.55726514
N 6.16393471 3.09846922 10.70153200
C 5.83933478 3.30246686 9.36740708
C 7.03858155 2.71170568 7.26469175
H 6.98314787 1.67532847 6.91718939
H 6.22414620 3.28068957 6.82478534
H 7.99655461 3.14195498 6.95852168
H 0.49810316 5.95685855 12.04103819
H 7.80431890 2.22181537 11.80952172
H 5.82887694 7.97869000 6.17464864
H 2.29411528 0.57241479 5.99587322
H 4.00624707 4.37214502 3.17931356
H 4.19414973 3.99439871 14.83179270
C 4.13612146 4.12086820 10.94475018
C 4.07459179 4.24569458 7.06618886

Carsetian Coordinates of **1b**:

63
FeC28N8H26

Fe 4.14765900 4.19116600 9.00441600
N 2.59147400 1.43450400 9.19774300
C 2.21369400 1.09230400 7.04546800
C 3.87408100 4.36795400 4.28270300
C 3.44680600 3.23241100 6.34129100
C 1.97956500 0.58396500 8.28107600
H 1.45124900 -0.30256200 8.59136700
C 3.33267000 3.26094400 4.95384700
H 2.84689100 2.46921000 4.39265300
N 2.95688700 2.24237800 7.24001600
C 3.19504400 2.46705800 8.57596800
C 2.52513000 1.25916800 10.64515200
H 1.65446500 1.77873200 11.05167900
H 3.42369300 1.67199600 11.09523800
H 2.45158600 0.19468000 10.87054900
N 5.73804200 6.90663400 9.22802200
C 5.88434200 7.42007700 7.08104400
C 4.59301700 5.32220300 6.35156400
C 6.24093200 7.83645800 8.32097200
H 6.79281700 8.70463100 8.64231500
C 4.51004600 5.41588800 4.96358400
H 4.91424300 6.25803300 4.41122900
N 5.17452000 6.24569200 7.26144800
C 5.07885700 5.91492100 8.59481600
C 5.94604800 6.98072200 10.66921700
H 6.97206300 6.69789200 10.91799500
H 5.25549500 6.29516000 11.15348300
H 5.75833400 7.99960100 11.01265300
N 1.23424000 5.42754600 8.82733200
C 0.74523600 5.48875400 10.98366200
C 4.08454700 3.92866000 13.72996400
C 3.03295900 4.54781200 11.67552000
C 0.23884900 5.73726000 9.75003400
H -0.72308500 6.11503600 9.44463600
C 2.97444900 4.47087800 13.06462000
H 2.11343700 4.81036500 13.63133100
N 2.03374600 5.02832900 10.78196400
C 2.34754400 4.98296700 9.44374900
C 1.06275100 5.50957800 7.38012300
H 0.31550800 6.27120900 7.15513500
H 2.01153400 5.77490100 6.92171800
H 0.73460800 4.54726300 6.98120800
N 7.05796200 2.99824600 8.76313600
C 7.50685400 2.69745000 10.90845200
C 5.21356400 3.58558800 11.65262500
C 8.03091300 2.57231300 9.66435700
H 8.99347800 2.21494800 9.33673000
C 5.21947200 3.47612500 13.04189200
H 6.05850600 3.05987600 13.59002200
N 6.22796800 3.19787300 10.73625900
C 5.93821200 3.39100200 9.40391700
C 7.25209800 3.04969200 7.31908700
H 7.68623500 2.10919300 6.97480200
H 6.28519600 3.20414600 6.84706600
H 7.92000100 3.87418800 7.05711800
H 0.31301700 5.61022700 11.96281200
H 7.92193400 2.47207400 11.87660700
H 6.06453100 7.85211600 6.11085900
H 1.93285100 0.73442800 6.06905600
H 3.79827300 4.41432000 3.20212000
H 4.06401400 3.85749400 14.81165600
C 4.13671700 4.11440400 10.96244000
C 4.07024600 4.24601800 7.04727600

Carsetian Coordinates of **2**:

91
FeB2C36N12H40

Fe 7.67328700 7.28249200 11.00503600
N 10.44925900 6.53445800 11.71232200
N 9.00167300 4.70396600 10.75736100
N 8.72089300 5.49574500 13.12489100
N 7.58178900 4.82666600 9.13164000
N 10.45805400 8.61785900 11.12583200
N 7.02137500 6.56384800 13.93209500
C 11.71881100 7.02051900 11.95905100
H 12.49801000 6.41019700 12.38044400
C 7.73844800 6.37026100 12.79485400
C 6.54083100 5.27460400 8.21783000
H 6.27088400 6.29768700 8.45286000
H 5.65570700 4.64104100 8.31232400
H 6.90552500 5.22436200 7.18960500
C 7.58362300 5.85178700 14.98363000
H 7.16708800 5.87445500 15.97756100
C 11.73316900 8.32578600 11.58441400
H 12.52218300 9.06026700 11.59076200
C 8.05876500 5.50019500 10.20897900
C 9.65808500 7.52586400 11.23415100
C 10.06211800 9.93627200 10.64983900
H 9.92582500 10.62324400 11.48827000
H 9.12564900 9.85203800 10.10816200
H 10.83652500 10.32661200 9.98703000
C 8.22568600 3.60257600 9.01099300
H 7.99244800 2.90867900 8.21964000
C 8.65354700 5.19284400 14.47410000
H 9.36693100 4.54800000 14.95607600
C 12.51543000 1.72810500 12.84010400
H 13.16698200 0.87663300 13.00690100
C 10.41902300 2.87038100 13.20842300
H 9.42288900 2.85318600 13.63714400
C 5.86639300 7.43665500 14.08976600
H 5.47646100 7.69311000 13.10992900
H 6.14747100 8.35520900 14.61047900
H 5.09724800 6.91788400 14.66526400
B 9.80269000 5.13466400 12.04442400
C 11.25069500 1.77178200 13.42387700
H 10.90718400 0.94622900 14.03931200
C 12.08532300 3.87218500 11.81435200
H 12.41372100 4.65179200 11.13534900
C 10.82287600 3.96398900 12.42438900
C 12.92603400 2.77908900 12.02201700
H 13.89681700 2.74386400 11.53759800
C 9.11665900 3.53275500 10.03361100
H 9.81726000 2.76206500 10.30701700
N 4.89730100 8.03056500 10.29781300
N 6.34494700 9.86104300 11.25271100
N 6.62567000 9.06923700 8.88519400
N 7.76483600 9.73829600 12.87842300
N 4.88846200 5.94718100 10.88436100
N 8.32523100 8.00121400 8.07798200
C 3.62774300 7.54452200 10.05108400
H 2.84854300 8.15485500 9.62970800
C 7.60813500 8.19474000 9.21522300
C 8.80576500 9.29029600 13.79223500
H 9.07554700 8.26714800 13.55728900
H 9.69098000 9.92371800 13.69764100
H 8.44111700 9.34069300 14.82046900
C 7.76295900 8.71326700 7.02645600
H 8.17951600 8.69065400 6.03253300
C 3.61335300 6.23927100 10.42577100
H 2.82431900 5.50481200 10.41945400
C 7.28783700 9.06478800 11.80108800
C 5.68846800 7.03914400 10.77596500
C 5.28430100 4.62879400 11.36051300

H 5.42046000 3.94169200 10.52216800
H 6.22081000 4.71300600 11.90212000
H 4.50990100 4.23862400 12.02343100
C 7.12101400 10.96242900 12.99904900
H 7.35430100 11.65633000 13.79038400
C 6.69300900 9.37216200 7.53599200
H 5.97959900 10.01698100 7.05402100
C 2.83100800 12.83677100 9.16995700
H 2.17940100 13.68820100 9.00315500
C 4.92744400 11.69456700 8.80157400
H 5.92354300 11.71178300 8.37277000
C 9.48028600 7.12850300 7.92031200
H 9.87026300 6.87211000 8.90014700
H 9.19928200 6.20991000 7.39962800
H 10.24937200 7.64732800 7.34478300
B 5.54389600 9.43034100 9.96566700
C 4.09570600 12.79312200 8.58611500
H 4.43915100 13.61865100 7.97061100
C 3.26126400 10.69275500 10.19578400
H 2.93293200 9.91315000 10.87482300
C 4.52369900 10.60099700 9.58570000
C 2.42049400 11.78579800 9.98811300
H 1.44972800 11.82099400 10.47256800
C 6.23001800 11.03226800 11.97645300
H 5.52944200 11.80298500 11.70305700

References

1. G. R. Fulmer, A. J. M. Miller, N. H. Sherden, H. E. Gottlieb, A. Nudelman, B. M. Stoltz, J. E. Bercaw and K. I. Goldberg, *Organometallics*, 2010, **29**, 2176-2179.
2. K. S. Kjær, N. Kaul, O. Prakash, P. Chábera, N. W. Rosemann, A. Honarfar, O. Gordivska, L. A. Fredin, K.-E. Bergquist, L. Häggström, T. Ericsson, L. Lindh, A. Yartsev, S. Styring, P. Huang, J. Uhlig, J. Bendix, D. Strand, V. Sundström, P. Persson, R. Lomoth and K. Wärnmark, *Science*, 2019, **363**, 249-253.
3. C. E. Johnson, J. Schwarz, M. Deegbey, O. Prakash, K. Sharma, P. Huang, T. Ericsson, L. Häggström, J. Bendix, A. K. Gupta, E. Jakubikova, K. Wärnmark and R. Lomoth, *Chem. Sci.*, 2023, **14**, 10129-10139.
4. R. K. Hocking, E. C. Wasinger, F. M. F. de Groot, K. O. Hodgson, B. Hedman and E. I. Solomon, *J. Am. Chem. Soc.*, 2006, **128**, 10442-10451.
5. R. Kurian, K. Kunnus, P. Wernet, S. M. Butorin, P. Glatzel and F. M. F. de Groot, *J. Phys.: Condens. Matter*, 2012, **24**, 452201.
6. K. Kunnus, M. Guo, E. Biasin, C. B. Larsen, C. J. Titus, S. J. Lee, D. Nordlund, A. A. Cordones, J. Uhlig and K. J. Gaffney, *Inorg. Chem.*, 2022, **61**, 1961-1972.
7. A. W. Hahn, B. E. Van Kuiken, V. G. Chilkuri, N. Levin, E. Bill, T. Weyhermüller, A. Nicolaou, J. Miyawaki, Y. Harada and S. DeBeer, *Inorg. Chem.*, 2018, **57**, 9515-9530.
8. M. O. J. Y. Hunault, Y. Harada, J. Miyawaki, J. Wang, A. Meijerink, F. M. F. de Groot and M. M. van Schooneveld, *J. Phys. Chem. A*, 2018, **122**, 4399-4413.
9. C. B. Larsen, J. D. Braun, I. B. Lozada, K. Kunnus, E. Biasin, C. Kolodziej, C. Burda, A. A. Cordones, K. J. Gaffney and D. E. Herbert, *J. Am. Chem. Soc.*, 2021, **143**, 20645-20656.
10. K. Kunnus, W. Zhang, M. G. Delcey, R. V. Pinjari, P. S. Miedema, S. Schreck, W. Quevedo, H. Schröder, A. Föhlisch, K. J. Gaffney, M. Lundberg, M. Odelius and P. Wernet, *J. Phys. Chem. B*, 2016, **120**, 7182-7194.
11. R. K. Hocking, E. C. Wasinger, Y.-L. Yan, F. M. F. deGroot, F. A. Walker, K. O. Hodgson, B. Hedman and E. I. Solomon, *J. Am. Chem. Soc.*, 2007, **129**, 113-125.
12. Y. Tanabe and S. Sugano, *J. Phys. Soc. Jpn.*, 1954, **9**, 753-766.
13. M. U. Delgado-Jaime, K. Zhang, J. Vura-Weis and F. M. F. de Groot, *Journal of Synchrotron Radiation*, 2016, **23**, 1264-1271.
14. C. Van Stappen, B. E. Van Kuiken, M. Mörtel, K. O. Ruotsalainen, D. Maganas, M. M. Khusniyarov and S. DeBeer, *Inorg. Chem.*, 2024, **63**, 7386-7400.
15. E. Stavitski and F. M. F. de Groot, *Micron*, 2010, **41**, 687-694.
16. K. Kunnus, L. Li, C. J. Titus, S. J. Lee, M. E. Reinhard, S. Koroidov, K. S. Kjær, K. Hong, K. Ledbetter, W. B. Doriese, G. C. O'Neil, D. S. Swetz, J. N. Ullom, D. Li, K. Irwin, D. Nordlund, A. A. Cordones and K. J. Gaffney, *Chem. Sci.*, 2020, **11**, 4360-4373.

17. H.-H. Schmidtke, in *Optical Spectra and Chemical Bonding in Inorganic Compounds: Special Volume dedicated to Professor Jørgensen I*, eds. D. M. P. Mingos and T. Schönherr, Springer Berlin Heidelberg, Berlin, Heidelberg, 2004, DOI: 10.1007/b11303, pp. 19-35.
18. F. de Groot, *Coord. Chem. Rev.*, 2005, **249**, 31-63.
19. Y. Tanabe and S. Sugano, *J. Phys. Soc. Jpn.*, 1954, **9**, 766-779.
20. M. D. Kuz'min, A. Savoyant and R. Hayn, *J. Chem. Phys.*, 2013, **138**, 244308.
21. A. M. Fatta and R. L. Lintvedt, *Inorg. Chem.*, 1972, **11**, 88-92.
22. A. D. Becke, *Phys. Rev. A*, 1988, **38**, 3098-3100.
23. S. Grimme, *J. Comput. Chem.*, 2006, **27**, 1787-1799.
24. M. Dolg, U. Wedig, H. Stoll and H. Preuss, *J. Chem. Phys.*, 1987, **86**, 866-872.
25. R. Krishnan, J. S. Binkley, R. Seeger and J. A. Pople, *J. Chem. Phys.*, 1980, **72**, 650-654.
26. A. D. McLean and G. S. Chandler, *J. Chem. Phys.*, 1980, **72**, 5639-5648.
27. S. I. Gorelsky, *AOMix: Program for Molecular Orbital Analysis*, 1997.
28. M. J. Frisch, G. W. Trucks, H. B. Schlegel, G. E. Scuseria, M. A. Robb, J. R. Cheeseman, G. Scalmani, V. Barone, G. A. Petersson, H. Nakatsuji, X. Li, M. Caricato, A. V. Marenich, J. Bloino, B. G. Janesko, R. Gomperts, B. Mennucci, H. P. Hratchian, J. V. Ortiz, A. F. Izmaylov, J. L. Sonnenberg, Williams, F. Ding, F. Lipparini, F. Egidi, J. Goings, B. Peng, A. Petrone, T. Henderson, D. Ranasinghe, V. G. Zakrzewski, J. Gao, N. Rega, G. Zheng, W. Liang, M. Hada, M. Ehara, K. Toyota, R. Fukuda, J. Hasegawa, M. Ishida, T. Nakajima, Y. Honda, O. Kitao, H. Nakai, T. Vreven, K. Throssell, J. A. Montgomery Jr., J. E. Peralta, F. Ogliaro, M. J. Bearpark, J. J. Heyd, E. N. Brothers, K. N. Kudin, V. N. Staroverov, T. A. Keith, R. Kobayashi, J. Normand, K. Raghavachari, A. P. Rendell, J. C. Burant, S. S. Iyengar, J. Tomasi, M. Cossi, J. M. Millam, M. Klene, C. Adamo, R. Cammi, J. W. Ochterski, R. L. Martin, K. Morokuma, O. Farkas, J. B. Foresman and D. J. Fox, Gaussian 16 Rev. C.01, 2016.